

Received November 3, 2020, accepted November 22, 2020, date of publication December 7, 2020, date of current version December 18, 2020.

Digital Object Identifier 10.1109/ACCESS.2020.3042798

Radar Signatures of Drones Equipped With Heavy Payloads and Dynamic Payloads Generating Inertial Forces

SAMIUR RAHMAN¹, (Member, IEEE), DUNCAN A. ROBERTSON¹, (Member, IEEE), AND MARK A. GOVONI², (Senior Member, IEEE)

¹School of Physics and Astronomy, University of St Andrews, St Andrews KY16 9SS, U.K.

²U.S. Army Research Laboratory, Adelphi, MD 20783, USA

Corresponding author: Samiur Rahman (sr206@st-andrews.ac.uk)

This work was supported by the Army Research Laboratory under Cooperative under Grant W911NF-19-2-0075.

ABSTRACT Due to the availability of cheap commercial and customizable drones, the potential for using them to carry threat payloads has increased significantly. In this study, radar signatures of drones carrying simulated threat payloads have been investigated experimentally. Two different scenarios were considered: 1) drones carrying heavy payloads and 2) the dynamic response of a drone subject to inertial recoil forces which mimic the effect of a firearm attached to the drone. Experimental data for the two scenarios was collected with 24 and 94 GHz Doppler radar systems. Micro-Doppler analysis has revealed that (i) the degree of fluctuation in helicopter rotor modulation (HERM) lines in long integration spectrograms does not correlate with the presence or absence of a heavy payload and (ii) the blade flashes in fully sampled, short integration spectrograms confirm that the tip velocity and rotation rate increase with payload weight as extra thrust is required. However, in both cases, these effects are difficult to attribute exclusively to the presence of the heavy payloads as they can also be attributed to other factors affecting flight dynamics such as wind or platform maneuvers. Finally, we present what we believe to be the first measurements of a simulated recoil scenario in which distinct signatures in the bulk Doppler of the fuselage are clearly attributable to the applied recoil. Analysis shows that these signatures are consistent with the inertial forces which would be imparted by a 9 mm parabellum round fired from a Glock 22 pistol if it was attached to the drone.

INDEX TERMS Radar, threat payload, recoil, FMCW, CW, millimeter wave.

I. INTRODUCTION

Drone technology has advanced significantly in recent years, allowing for numerous useful applications. However, it also poses a security threat if being used with malicious intent [1], [2]. As a result, research on drone detection and classification technology has grown considerably. Radar has the ability to operate in all-weather conditions, hence is used as one of the one of the main sensors for counter drone technology. Numerous research works have been published [3]–[7]. The radar based solutions mostly rely on the micro-Doppler signatures produced by the return signal from the drone propeller blades [8], [9]. Despite the broad literature, there are very few reports specifically considering the radar signatures of drones carrying threat payloads. In [10], S-band multistatic radar data of a DJI Phantom Vision 2+ was

collected, in which the drone was hovering without a payload and also with a 500 g payload attached. It was shown that different micro-Doppler signatures were observed in those two cases and a classification algorithm was proposed to distinguish between a drone with and without a payload. In [11], a deep learning classification technique (Convolutional Neural Network) was applied to the same dataset as [10] with very good results. Some initial payload classification results based on micro-Doppler signatures are also reported in [12].

Our objective in this work has been to gain a much more extensive and deeper understanding of the radar signatures of drones equipped with different threat payloads. We have intentionally omitted any analysis based on theory/simulation as the main novelty of the paper lies in the experimental data showing the radar signatures of drones with simulated threat payloads in various conditions. Our view is that realistic experimental data collection and analysis, even using simulated threat payloads, provides more realistic and valuable

The associate editor coordinating the review of this manuscript and approving it for publication was Julien Le Kerneec¹.

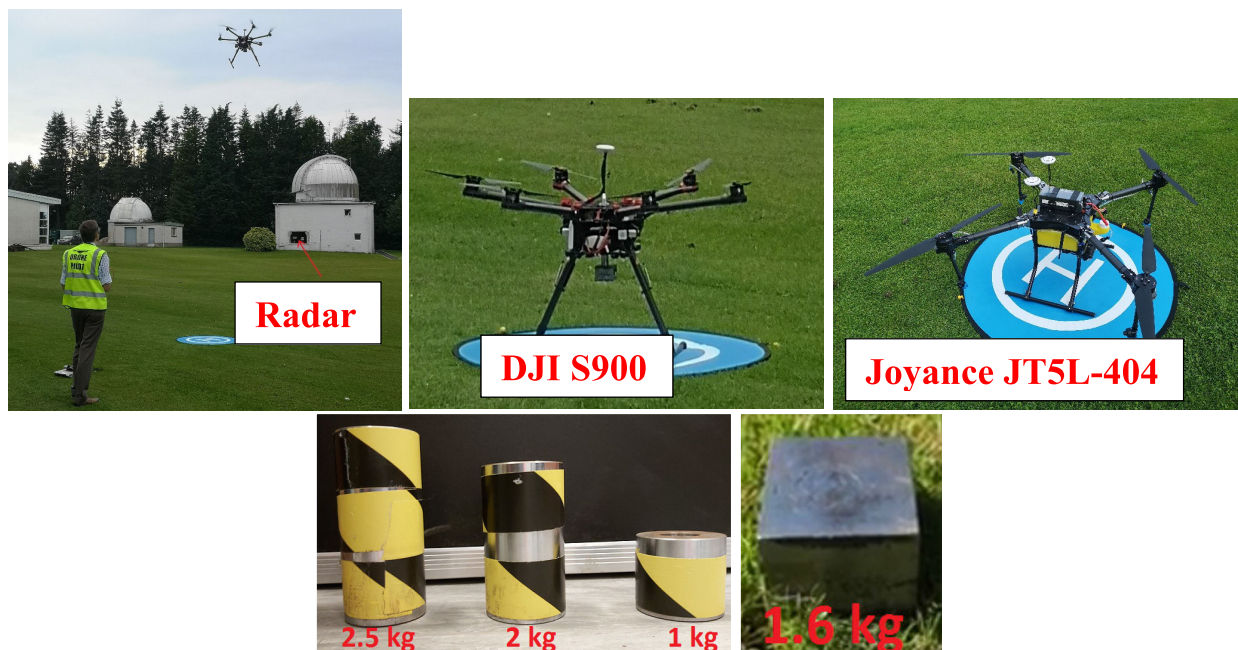


FIGURE 1. Illustration of the experimental scenario and the drones (S900 with electromagnet payload attachment, JT5L-404 with 5 liter water tank) and steel payloads used with the S900 during the trial.

information than can be obtained from modelling. Simulation of such dynamic scenarios requires detailed knowledge of dynamic behavior of the drone's flight controller but this is proprietary information of the manufacturer and is not readily accessible. Any modelling done without incorporating accurate flight dynamics under perturbation (due to payload or recoil) will not be very reliable. We believe our experimental approach yields results which are more realistic and directly applicable to the design of radar systems for detecting drones with threat payloads. Hence, in this study, we gathered a large dataset with varying parameters: a) trials on different days to assess wind effects; b) modifying a drone to remotely release payloads to gather signatures of payload release; c) using different payload weights to analyze the impact of weights; d) gathering data from two different drones to observe generic patterns; e) gathering data obtained at two different radar frequencies; and f) obtaining both CW and FMCW radar data. According to our knowledge, the following are the two main novel aspects of this study:

1. This is the first report on the radar signatures of drones equipped with heavy payloads based on a large set of diverse experimental results.
2. This is the first report on the radar signatures of the recoil effect mimicking a firearm attached to a drone.

In the first part of this study, we have performed more elaborate experimental trials to obtain radar signatures of drones with heavy payloads. A drone was modified to carry a payload which could be released remotely so that the transient analysis could be performed. Data was collected using four different weights to better understand the changes in micro-Doppler signatures. The maximum payload capacity of the modified drone could carry was 3 kg but we used payload weights up to 2.5 kg to ensure the drone remained

stable in-flight. In the second part, we report on the experimental data analysis of the radar signatures of drones perturbed by a brief external force, simulating the effect of a gun attached to the drone and firing a shot. According to our knowledge, there is no prior literature available on this topic. All the data for this study was obtained using high frequency radar systems (K-band and W-band) which provide high fidelity micro-Doppler measurements [13]. Data was post processed in MATLAB[®] to analyze the return signal characteristics.

II. HEAVY PAYLOADS

Our main goal was to investigate the change in radar signature due to the presence of an attached heavy payload. Subsequently, we examined whether the change in the signature is unique to the payload so that a classification decision can be made with high confidence. We investigated two cases: i) payloads rigidly attached to the fuselage of the drone and ii) payloads attached to the drone fuselage with a wire to create a pendulum effect.

A. PAYLOAD ATTACHED RIGIDLY TO FUSELAGE

A DJI S900 hexacopter was fitted with an electromagnet to which we attached steel payloads with weights of 1, 1.6, 2 and 2.5 kg. The electromagnet can be disabled by the drone controller allowing the payload to be released in a controlled way during flight. A Joyance JT5L-404 crop spray quadcopter was also used for payload experiments. This drone carries a 5 liter water tank (i.e. a 5 kg payload). Data was taken of this drone with the water tank both filled and empty. Fig. 1 shows the experimental scenario, the two drones and the four steel payloads. The 24 GHz radar [14] and the 94 GHz radar [15] collected staring data simultaneously. The 24 GHz radar is a coherent radar with +24 dBm transmit

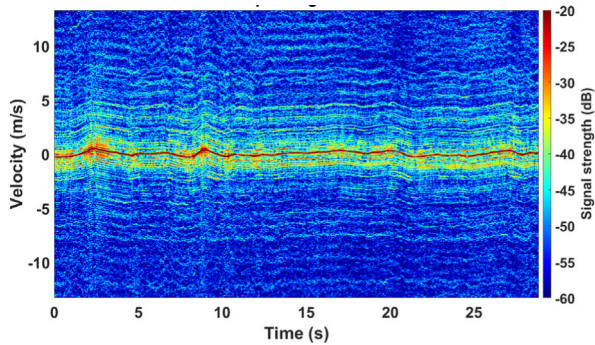


FIGURE 2. Example 24 GHz FMCW spectrogram of S900 hovering with a 1.6 kg payload attached when the wind speed was ~12 mph, showing fluctuation in the bulk Doppler and HERM lines.

power, linear horizontal polarization and an antenna beam width of 11.2° in both azimuth and elevation. The 94 GHz radar is a very low phase noise coherent radar with +18 dBm transmit power, circular polarization and the antenna beam width is 0.97° in azimuth and 3° in elevation. For these experiments, the 24 GHz radar was operated in FMCW mode to provide range and Doppler data and the 94 GHz radar was operated in CW mode to provide non-aliased Doppler data and because the Doppler sensitivity is greater at the higher frequency [13]. Data was collected on four different days. On the first two days the wind speed was greater than 10 mph but was less than 5 mph on the last two days. The drones were flown 20-60 m away from the radars at altitudes of 5-8 m.

1) FMCW DATA

We begin by describing the 24 GHz FMCW results. We wanted to observe the helicopter rotor modulation (HERM) lines in the spectrograms, so used a longer window in the Short Time Fourier Transform (STFT) for better frequency resolution. All the FMCW data processing in this case was done with a coherent processing interval (CPI) length of 2048 chirps, corresponding to 480.9 milliseconds, which yields a Doppler resolution of 2.1 Hz or 0.013 ms^{-1} (at 24 GHz). The chirp repetition frequency (CRF) was 4.26 kHz.

In Fig. 2, the spectrogram is obtained from data taken with the S900 hovering with the 1.6 kg payload attached when the wind was quite strong (~ 12 mph). It is seen that there is a significant fluctuation in the bulk Doppler signature as the drone was trying to stabilize itself continuously. The fluctuations in the HERM lines corresponding to the micro-Doppler signatures are also observed to be quite random.

To reduce the effect of wind, data was collected on a day with the wind speed < 5 mph and spectrograms for the S900 are shown in Fig. 3. All these spectrograms are also shown having been bulk Doppler aligned by tracing the strongest signal offset from the zero Doppler in each vertical slice which is due to the fuselage bulk Doppler and then shifting the array accordingly. This enables a better visualization of the HERM line fluctuations irrespective of the bulk motion. In all cases, the drone was hovering with a payload attached which was released after a few seconds. The payload release time values were recorded manually, hence

are only accurate to around ± 1 s. In Fig. 3(a) the drone was hovering with a 1 kg payload attached which was released at $t \approx 15$ s. Also, the drone flew off and out of the antenna beam from $t = 20$ s. There is no significant difference in the shape of the HERM lines with and without the payload. Fig. 3(b) shows the spectrogram plots when the payload weight was 1.6 kg. Payload release time was $t \approx 28$ s. It can be seen that there are regions of fluctuation and stability in both cases (before and after the payload release). In Fig. 3(c) the drone was carrying a 2 kg payload and made a small manoeuvre between $t \approx 17$ s and $t \approx 22$ s. There is a small perturbation in the HERM lines around the time the payload was released at $t \approx 10$ s but otherwise there is little difference with and without the 2 kg payload. Finally, Fig. 3(d) shows the spectrogram of the drone carrying a 2.5 kg payload which was released at $t \approx 20$ s and the drone started flying away at $t \approx 23$ s. Just like the previous results, no unique HERM line characteristic is observed that would directly correspond to the presence or absence of the payload.

Fig. 4 shows the spectrograms of the signal return from the Joyance, both with tank empty and full of water. It is seen that the micro-Doppler signatures fluctuated more when the 5 kg payload was present than when it was absent.

All these spectrograms from two different drones and multiple weights of payload show that the HERM lines and bulk Doppler signatures tend to fluctuate both with and without payload. During our experiments we noted that both drones appeared to struggle to maintain position and stability with heavier payloads and this tended to improve when the payload was absent. The ability to release the payload on the S900 in mid-air enabled a rapid comparison between payload and no payload. However, whilst a change was obvious in some measurement runs it was not universally evident in all FMCW Doppler spectrograms. Also, there was no clear cut way of distinguishing fluctuations due to the presence of payloads from fluctuations due to the effect of wind, which also causes the flight controller to continuously adjust the positional coordinates. There did not seem to be a consistent correlation between the straightness of the HERM lines and the presence of a heavy payload.

These results suggest that the visual presence, or lack of, fluctuations in HERM lines is not a definitive signature to determine the presence of a payload and would not provide the basis for a robust classification. The degree to which the HERM lines fluctuate can be due to more than one factor, particularly the wind and its effect on the dynamic behaviour of the flight controller. It should be noted that this conclusion differs from the results reported in [10], where a visual difference between the HERM line pattern was observed (lines appeared straighter with a payload present) which may be due to the different type of drone used for that study.

a: PAYLOAD CLASSIFICATION

As a visual discrimination could not be made, we have further analyzed the results using machine learning techniques to find out if there is any hidden feature present. At first, we

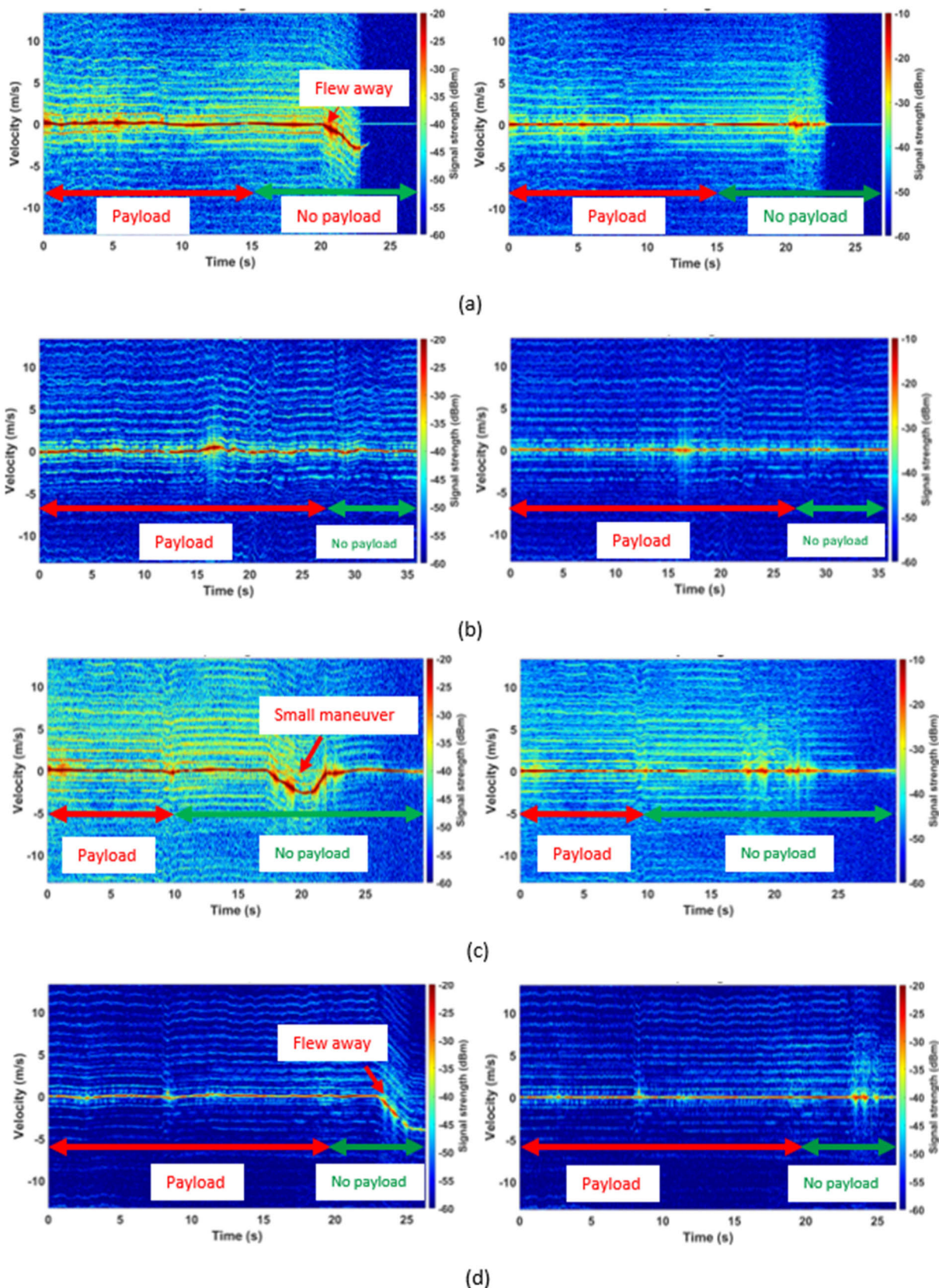


FIGURE 3. Example 24 GHz FMCW spectrograms of S900 hovering in low wind (~5 mph) with a) 1.0 kg payload attached then released at $t \approx 15$ s (left) and after bulk Doppler alignment (right), b) 1.6 kg payload attached then released at $t \approx 28$ s (left) and after bulk Doppler alignment (right), c) 2.0 kg payload attached then released at $t \approx 10$ s (left) and after bulk Doppler alignment (right), d) 2.6 kg payload attached then released at $t \approx 20$ s (left) and after bulk Doppler alignment (right).

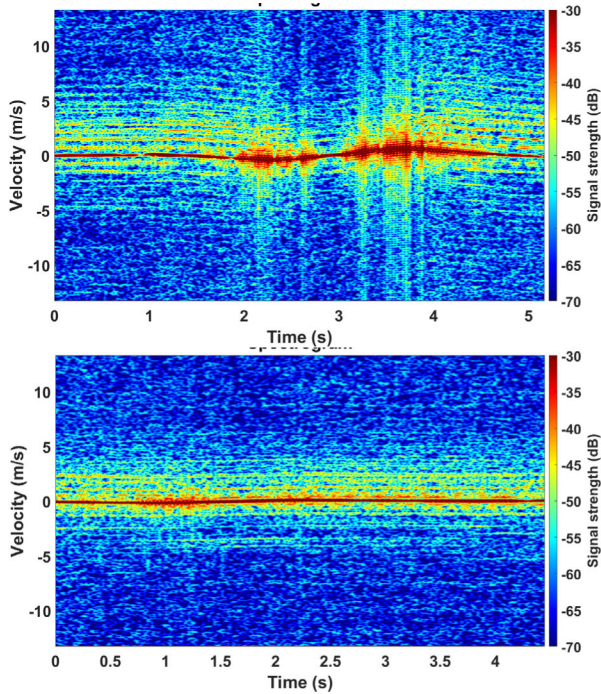


FIGURE 4. Example 24 GHz FMCW spectrogram of JT5L-404 hovering with 5.0 kg payload (top) and without payload (bottom).

performed feature extraction based training to determine the presence of payload. Then, we have also used a pre-trained neural network (GoogLeNet) to examine the classification performance.

i) FEATURE EXTRACTION BASED CLASSIFICATION

For automatic target recognition, feature extraction based machine learning machine learning techniques can deliver robust performances. The main challenge usually is to select the relevant features from the datasets, which would provide the best contrast among the different classes of targets.

The use of Doppler features for classifying a drone is quite widely used [3], [4], [16], [17]. In [16], we used four different features related to micro-Doppler signatures to classify between a drone and a bird, where 100% classification accuracy was achieved. In the case of payload classification, we have modified the features since HERM lines play a more important role in this case. The feature value extractions are mainly done by using singular value decomposition (SVD). Considering a spectrogram matrix as SF , the SVD of SF will then be $SVD(SF) = USV^T$. Here, S is the diagonal matrix, which shows the weights of every column. Higher weight entails more information in that column. The U matrix corresponds to the vertical axis information, in this case it is the Doppler axis of the spectrogram. On the other hand, the V matrix corresponds to the horizontal axis information, in this case it is time information, which can be used to investigate the temporal behaviour of the HERM lines. The features are discussed below:

1. Doppler spread weight. Measures the area under the curve of the Doppler spread [16]. To measure the Doppler spread, SVD is performed on the spectrogram SF first. The

Algorithm 1 Doppler Spread Weight Feature Value

1. **Input:** $SF(i,j); i = 1, 2, \dots, I; j = 1, 2, \dots, J$
2. **SVD:** $SVD[SF] = USV^T$
3. **Output:** $DSW = \sum_{i=1}^I \vec{u}_i;$
 $\vec{u}_i \rightarrow$ first row vector of U

Algorithm 2 Doppler Strength Feature Value

1. **Input:** $SF(i,j); i = 1, 2, \dots, I; j = 1, 2, \dots, J$
2. **Output:** $DS = \sum_{i=1}^I \sum_{j=1}^J SF(i,j)$

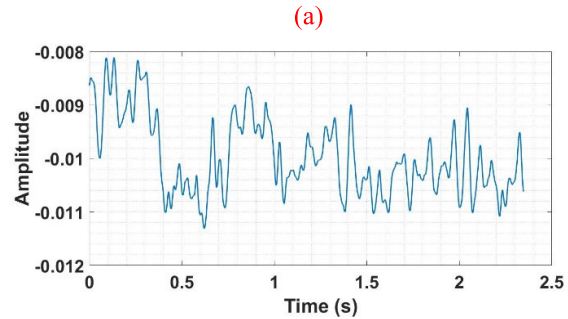
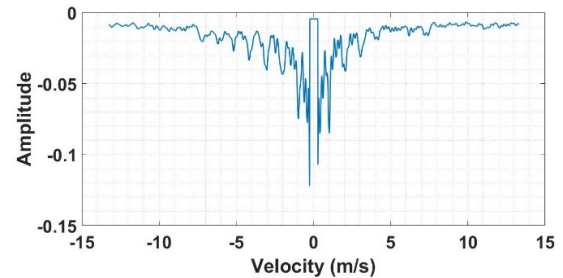


FIGURE 5. Example first row vectors after performing SVD for HERM line feature extraction, (a) first row vector of U matrix and (b) first row vector of V matrix.

spectrogram contains I and J number of data points on the Doppler and the time axes, respectively. The first row vector of the U matrix is selected and the area under the curve is then calculated, which is used as the feature value. The first row vector is used as it was determined from the diagonal S matrix that only this row contains significant information. The algorithm to obtain the feature value is summarized in Algorithm 1.

2. Doppler strength. This measures the overall strength of the micro-Doppler spectrogram [16]. In practice, the elements corresponding to the zero Doppler and its close vicinity are omitted, to exclude the contributions from the fuselage. The algorithm to obtain the feature value is summarized in Algorithm 2.

3. HERM line spacing. Calculated by taking the first row vector of the U matrix and then finding the peak locations. The mean spacings between adjacent peaks have been calculated for the feature value. Fig. 5(a) shows an example of the

Algorithm 3 HERM Line Spacing Feature Value

1. **Input:** $SF(i,j); i = 1, 2, \dots, I; j = 1, 2, \dots, J$
2. **SVD:** $SVD[SF] = USV^T$
3. **Peak search:** $p(k) = \text{findpeaks}[\vec{u}];$
 $\vec{u} \rightarrow$ first row vector of $U; k = 1, 2, \dots, K;$
 $K =$ number of peaks
4. **Output:** $HS = \text{mean}[p(k)]$

Algorithm 4 HERM Line Fluctuation Feature Value

1. **Input:** $SF(i,j); i = 1, 2, \dots, I; j = 1, 2, \dots, J$
2. **SVD:** $SVD[SF] = USV^T$
4. **Output:** $HF = \text{StdDev}[\vec{v}]$
 $\vec{v} \rightarrow$ first row vector of V

first row vector of the U matrix, from which the HERM line spacing feature value is calculated.

Note that in practice the peaks become very small and indistinguishable at larger Doppler/velocity values, as seen in Fig. 5(a) so only the peaks within $\pm 8 \text{ ms}^{-1}$ are considered. The algorithm to obtain the feature value is summarized in Algorithm 3.

4. HERM line fluctuation. Calculated by taking the first row vector of the V matrix and then calculating the standard deviation of the vector as the feature value. In Fig. 5(b), an example is shown of the first row vector of the V matrix, where the fluctuation directly corresponds to the HERM line fluctuation over time. The algorithm to obtain the feature value is summarized in Algorithm 4.

After obtaining the feature values, training was performed by very two very widely used classifiers, linear discriminant (LD) and support vector machine (SVM).

In the case of SVM, we have trained with both linear and quadrature SVM. We have performed training for two different cases; 2-class (payload, no payload) and 5-class (1 kg, 1.6 kg, 2 kg, 2.5 kg and no payload). All the trainings are done with 5 fold cross validation. Also, as the four features can be divided in to two sub groups (the last two specifically correspond to the HERM lines), we have trained by using (i) all four features, (ii) just the first two features and (iii) just the last two features. The detailed quantitative results are shown in table I. As seen from table 1, the classification performances range between 28% and 75%. A few scatter plots and confusion matrix plots are shown in Fig. 6 to provide some visual description of the training. It can be seen from Fig. 6(d) that the worst separation is for the no payload class. There was some feature separation observed with different payload weights, but no payload features are spread out more, significantly limiting the classification performance. This can be attributed to the fact that environmental effects (i.e. wind effect, flying etc.) were more diverse in the case of no payload data collection. Further work would be required to fully disambiguate the effects of the environment and any payload.

TABLE 1. Classification accuracy in terms of different classifier, feature and classification type (LD - Linear Discriminant, SVM - Support Vector Machine, HF - Herm Fluctuation, HS - Herm Spacing, DSW - Doppler Spread Weight, DS - Doppler Strength).

Classification type	Number of features	Classifier	Accuracy (%)
2 class	4	LD	57.1
2 class	4	Linear SVM	42.9
2 class	4	Quadrature SVM	71.4
2 class	2 (DSW, DS)	LD	28.6
2 class	2 (DSW, DS)	Linear SVM	28.6
2 class	2 (DSW, DS)	Quadrature SVM	50
2 class	2 (HF, HS)	LD	64.3
2 class	2 (HF, HS)	Linear SVM	50.0
2 class	2 (HF, HS)	Quadrature SVM	64.3
5 class	4	LD	72.1
5 class	4	Linear SVM	72.1
5 class	4	Quadrature SVM	67.4
5 class	2 (DSW, DS)	LD	65.1
5 class	2 (DSW, DS)	Linear SVM	67.4
5 class	2 (DSW, DS)	Quadrature SVM	74.4
5 class	2 (HF, HS)	LD	41.9
5 class	2 (HF, HS)	Linear SVM	48.8
5 class	2 (HF, HS)	Quadrature SVM	39.5

ii) NEURAL NETWORK BASED CLASSIFICATION

Using the spectrograms for neural network based classification of drones has been explored recently [7], [18]–[20]. In [18], we used convolutional neural network based training on a large labelled dataset of drones and birds to discriminate between the targets. The results showed very high classification accuracy ($>95\%$). For payload discrimination, we have again adopted this approach and used GoogLeNet [21]. The advantage of GoogLeNet is that it is already pre-trained; the lower level features (lines, curves etc.) need not be learned again, hence increasing the robustness of the training. Also, a large dataset is not mandatory while training with a pre-trained network. A large dataset eventually becomes useful to ensure the model is not overfitted but with a smaller dataset the method gives a very accurate indication of whether the model has found any distinct feature. Here, we have created labelled dataset of 2-class and 5-class targets as with the feature extraction based training, with each class containing 25 spectrogram images. The time duration of each spectrogram image is 2 seconds, which is just long enough to incorporate some temporal variation of the HERM lines. 80% of the data is used for training and 20% for validation.

The validation accuracy achieved for 5-class training is 58.82% and 50% for 2-class. In both cases, the loss function never approached zero, suggesting that the model was struggling to converge. This means that, again, no distinct feature was found by the model to robustly discriminate between payload/no payload scenarios.

2) CW DATA

To observe the propeller blade signature changes more accurately, the 94 GHz CW data was used. In this mode, a much

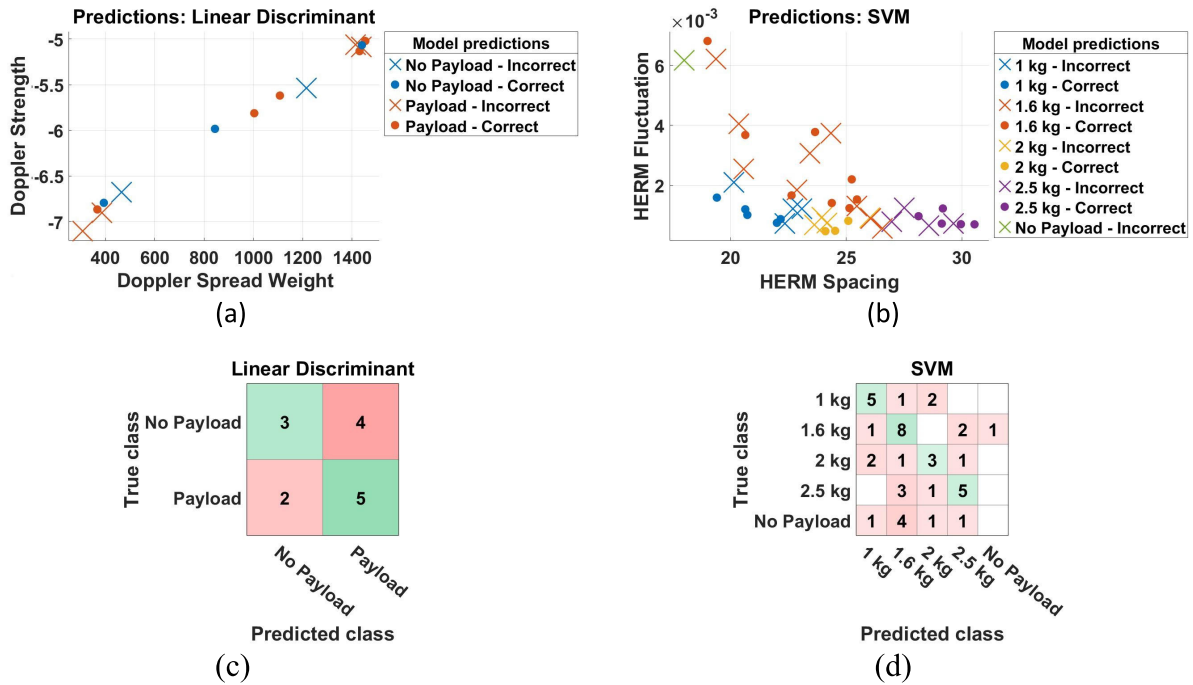


FIGURE 6. Example plots obtained during feature extraction based training, (a) scatter plot for 2-class using linear discriminant, (b) scatter plot for 5-class using SVM, (c) confusion matrix for 2-class using linear discriminant, (d) confusion matrix for 5-class using SVM.

higher Doppler sampling frequency can be used and enables the unambiguous sampling of the return signals from the very fast rotating propeller blades. The CW sampling rate was set to 200 kHz which gives a velocity range of $\pm 160 \text{ ms}^{-1}$ (at 94 GHz), sufficient for sampling the propeller tip velocities of both the S900 and Joyance. During signal processing, the CPI length was shorter than that used for the FMCW data to achieve better temporal resolution [22]. The STFT window length was 512 samples, corresponding to 2.56 milliseconds. The Doppler resolution then becomes 390 Hz or 0.62 ms^{-1} (at 94 GHz).

Fig. 7 shows example spectrogram plots of the S900 with and without payload. Here, the blade flashes are very distinct and appear as linear features in the velocity axis. The tip velocity is around 120 ms^{-1} with the 2.5 kg payload. It is noticed that the tip velocity decreases when the payload is released, falling to $\sim 100 \text{ ms}^{-1}$. This is expected as the propeller blades rotate faster, generating more lift, to support the weight of a payload. The same trend is observed in Fig. 8 for the Joyance, where the tip velocity is $\sim 100 \text{ ms}^{-1}$ with 5 kg payload (full tank) and $\sim 90 \text{ ms}^{-1}$ without payload.

It can be seen from Fig. 7 and Fig. 8 that the CW Doppler spectrograms reveal blade flashes from multiple propellers simultaneously. In general these will have different rotation rates so the temporal behavior of the blade flashes is complex. We have developed a signal processing workflow to analyze the spectrograms to determine the dominant rotational frequency and investigate how that changes with time and as a function of payload weight. The method for the CW Doppler data processing flow is presented in Algorithm 5. Firstly, a long time series data set ($S(n)$) obtained from a

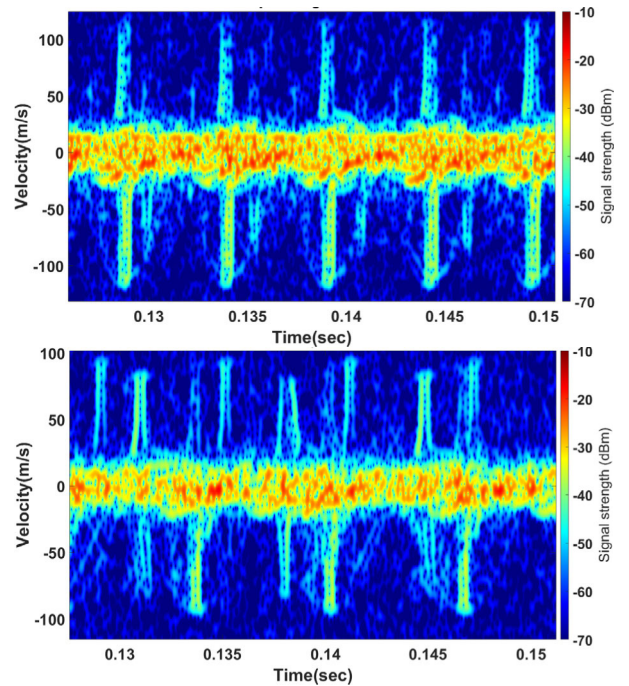


FIGURE 7. 94 GHz CW Doppler spectrogram of S900 hovering with 2.5 kg payload exhibiting a tip velocity of $\sim 120 \text{ ms}^{-1}$ (top) and without payload exhibiting a tip velocity of $\sim 100 \text{ ms}^{-1}$ (bottom).

measurement run is split into multiple short time segments of $\sim 300 \text{ ms}$ each from which spectrograms are generated. SVD is then applied to $\sim 50 \text{ ms}$ sub-sections of each spectrogram to reduce data dimensionality and to extract the propeller dominant rotational frequency ($\sim 50 \text{ ms}$ sub-sections are processed to reduce the computational load of this step). Only the SVD

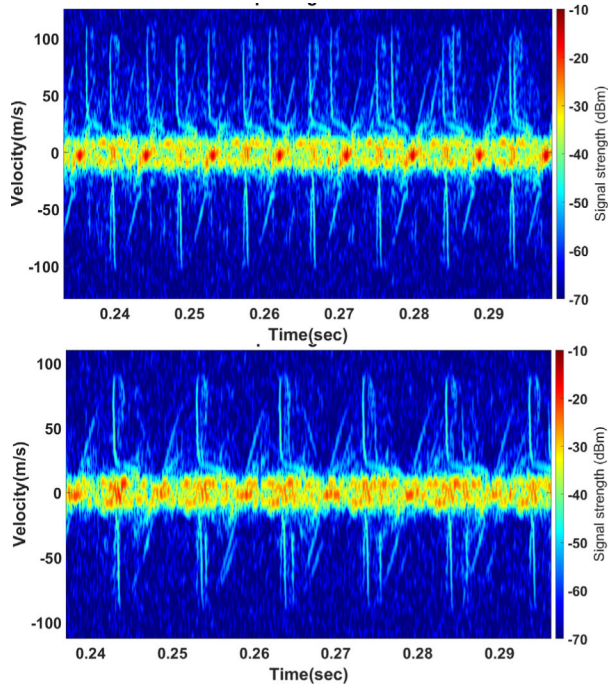


FIGURE 8. 94 GHz CW Doppler spectrogram of JT5L-404 hovering with 5.0 kg payload exhibiting a tip velocity of $\sim 100 \text{ ms}^{-1}$ (top) and without payload exhibiting a tip velocity of $\sim 90 \text{ ms}^{-1}$ (bottom).

Algorithm 5 Dominant Doppler Frequency

1. **Input:** $S(n); n = 1, 2, \dots, N$
2. **Data segmentation:** $s_1(m), s_2(m), \dots, s_M(m); m = 1, 2, \dots, \frac{N}{M}; M = \text{no. of segments}$
3. **Spectrogram generation:** $\text{sf}_1 = \text{STFT}[s_1], \text{sf}_2 = \text{STFT}[s_2], \dots, \text{sf}_M = \text{STFT}[s_M]$
4. **SVD:** $\text{SVD}[\text{sf}_1] = U_1 S_1 V_1^T, \text{SVD}[\text{sf}_2] = U_2 S_2 V_2^T, \dots, \text{SVD}[\text{sf}_M] = U_M S_M V_M^T$
5. **FFT:** $d_1(m') = \text{FFT}[\vec{v}_1(m)], d_2(m') = \text{FFT}[\vec{v}_2(m)], \dots, d_M(m') = \text{FFT}[\vec{v}_M(m)]; m' = 1, 2, \dots, \frac{M}{2}; \vec{v} \rightarrow \text{first row vector of } V$
6. **Peak search:**
$$D_{1, \dots, M} = \begin{cases} fd_{1, \dots, M}, & |d(m'_{fd})| > \text{thres.} \\ 0, & \text{otherwise} \end{cases}$$

 $fd = \text{fundamental frequency}$
7. **Output:** $DF = [D_1, D_2, \dots, D_M]$

V matrix (the time axis) is used as this contains the temporal information related to the blade flashes. The U matrix does not provide any time axis (hence rotation rate) information, so has not been used here. We then compute the Fourier transform of the V matrix to yield the frequency spectrum of the propeller dominant rotational frequency. Fig. 9 shows an example plot to illustrate the end result. Here, the dominant rotational frequency has changed from 160 Hz without payload to 200 Hz with 2.5 kg payload due to the increased thrust required to maintain lift. A threshold is then applied to

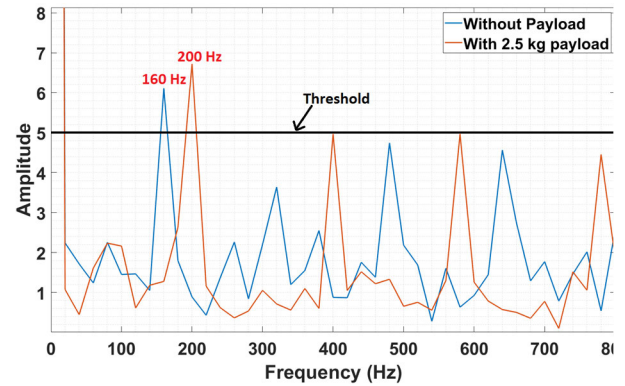


FIGURE 9. Example result of the SVD based dominant frequency determination process showing a frequency increase from 160 to 200 Hz due to the presence of a payload, measured at 94 GHz.

extract only the peak values associated with the fundamental component. The threshold is chosen as such so that a balance is maintained between detection and false alarms. As seen in Fig. 9, the threshold is chosen just above the maximum harmonic signal amplitudes, assuming that noise amplitude is unlikely to be larger than this, so larger signals will correspond to fundamental frequencies most of the time.

To test the robustness of the method, experimental data was collected for all the four S900 payload weights using the 94 GHz radar. In each case, the data was taken while the drone was hovering with the payload attached and then releasing it after a while. In Fig. 10 it is seen that the dominant frequency is consistently 160 Hz when the drone is hovering without payload. A sudden shift in frequency is observed when the payload is released for all the weights, but more clearly for the heavier weights, which is expected. The fluctuations at times other than when the payload release occurred can be attributed to the wind causing the drone to stabilize itself. From the values shown in Fig. 10, the correlation between the dominant rotational frequency and payload weight can be determined, which is illustrated in Fig. 11. The upward trend in frequency as weight increases is evident. The reason for the frequency not increasing beyond 200 Hz is not fully known, but may reflect that the drone motors have reached maximum speed / thrust.

It should be noted that these results rely on identifying a relative change in frequency compared to the base frequency for any particular drone (e.g. 160 Hz for our S900). The absolute value of base frequency will vary with drone type and its particular configuration / payload which could only be determined by collecting a large dataset or having *a priori* knowledge of the motor speeds for a wide variety of drones. In practice, this information is not likely to be available, so we suggest it would be very difficult to robustly determine the presence of a payload from knowing the absolute rotation frequency. The sudden change in rotation frequency when a payload is dropped can be detected during continuous measurement but this may be too late to provide actionable information. Also like the HERM lines in the FMCW results, there can be false alarms due to normal flight dynamics

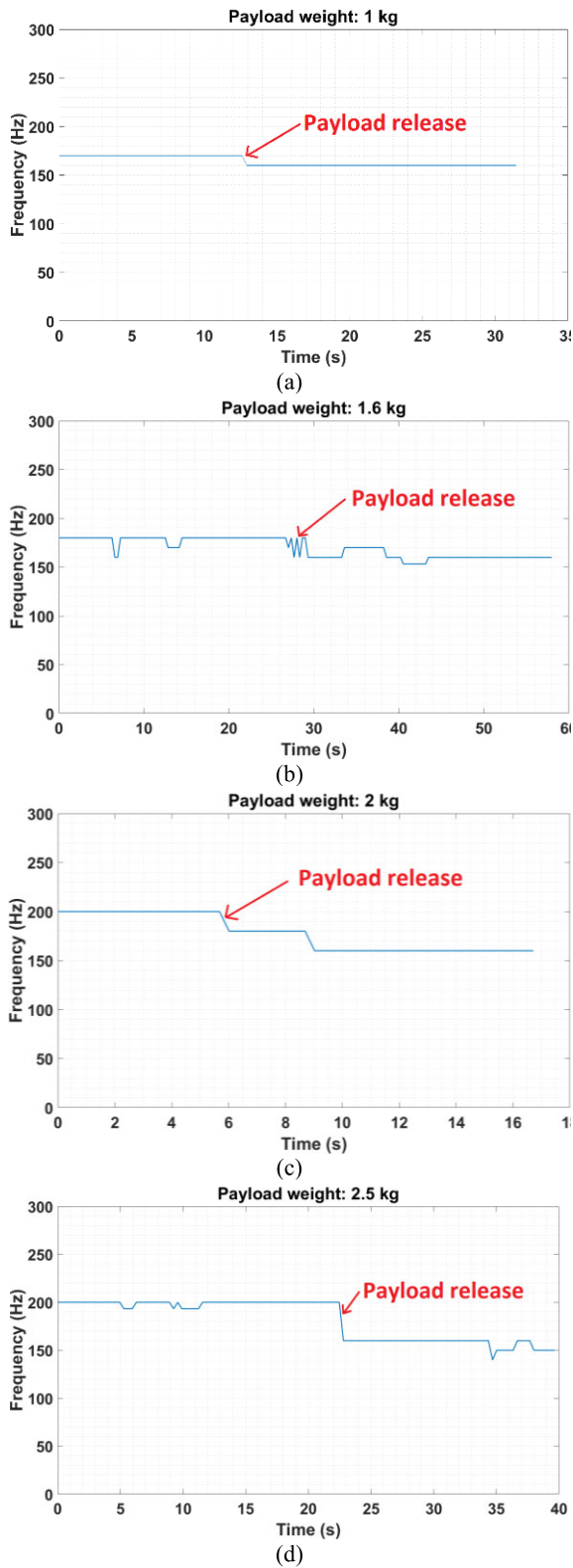


FIGURE 10. Trace of SVD based propeller dominant rotational frequency for S900 during payload release with payloads of (a) 1 kg, (b) 1.6 kg, (c) 2 kg, (d) 2.5 kg, measured at 94 GHz.

(wind or sudden acceleration) which exhibit similar changes in rotation frequency.

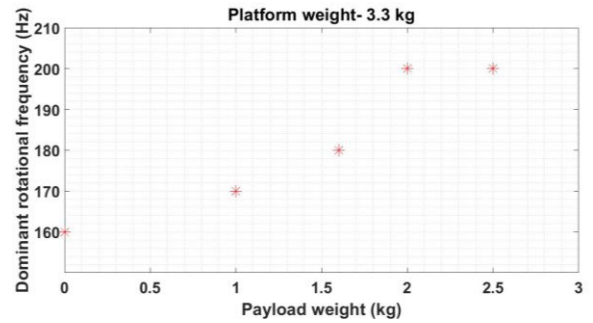


FIGURE 11. Propeller dominant rotational frequency for S900 vs attached payload weight, measured at 94 GHz.



FIGURE 12. S900 carrying 2 kg payload on 1 m wire for pendulum experiments.

B. PAYLOAD ATTACHED WITH A WIRE

Payloads attached with a wire were investigated using the S900 and the 1 and 2 kg payloads which were suspended from the drone on 0.6 and 1 m wires, as seen in Fig. 12. FMCW data was collected using the 94 GHz radar configured for 10 cm range bins. Whilst hovering or during normal maneuvers the wire attached payload hung directly below the drone and did not swing appreciably. It therefore tended to be positioned in the same range bin as the fuselage and was not easily resolved from the bulk return of the drone. By commanding sudden start/stop maneuvers to the drone the payload could be made to swing an appreciable amount for a short time, like a pendulum. The high range resolution of the radar could then resolve separate returns from the drone and the payload. Fig. 13 and Fig. 14 are examples of such an extreme case where the drone was intentionally jerked heavily by the flight controller. Fig. 13 shows an example range-Doppler plot for such a case in which the 2 kg payload was suspended on the 1 m wire below the S900 and made to swing. The radar boresight was pointed slightly below the fuselage towards the payload which reduced the micro-Doppler return from the propellers. The drone and payload are clearly resolved in this case. The spectrogram of Fig. 14 was generated from the FMCW data and the colour scale dynamic range was limited to suppress the low level micro-Doppler signals and emphasise the bulk Doppler signatures of the fuselage and payload. The sinusoidal velocity traces of the fuselage and payload are clearly seen to be in anti-phase. The signal from the payload is

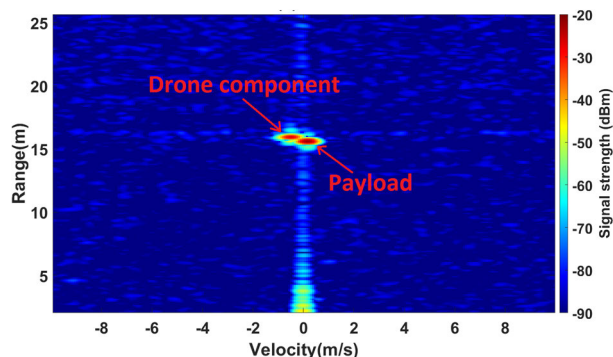


FIGURE 13. 94 GHz range-Doppler plot of 2 kg payload suspended on a 1 m wire below the S900 drone. 10 cm range resolution, with radar pointing slightly below the fuselage towards the payload.

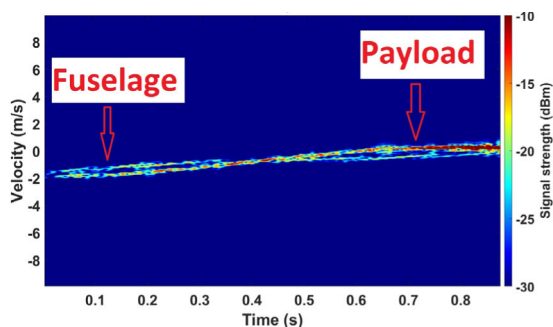


FIGURE 14. 94 GHz FMCW bulk Doppler spectrogram of S900 with 2 kg payload swinging from a 1 m wire.

stronger than the fuselage due to the antenna boresight being pointed slightly downwards towards the payload. The drone and the payload have bulk velocity vectors in the opposite direction to each other since the sudden acceleration of the drone caused the payload to swing in the opposite direction from the drone due to inertia. Here, the oscillatory signature is visually apparent, suggesting it could be used for classification. Still, it should be noted that this was achieved by inducing an extreme scenario which in practice is going to be an unlikely event. Hence, it is more realistic to make a conclusion in terms of general cases, where this phenomenon was not observed.

By considering the above circumstances, we conclude that there is no readily accessible, distinct, radar signature from a payload suspended below a drone.

III. DYNAMIC PAYLOADS

This section investigates the characteristic changes in the radar signature of the drone produced by the inertial force generated by a dynamic payload such as a gun. The goal is to determine a unique feature which can be used to identify the particular payload. The assumption is that a drone reacting to some payload-induced inertial force is likely to show a characteristic change in its kinematic behaviour and position as it jerks about then re-stabilises. This will correspond to recoil and counter-recoil, respectively.

We have focussed only on FMCW data collection in this case, as the recoil and counter-recoil effects will be apparent

from the bulk Doppler signature, not the micro-Doppler. It can be assumed that there will be micro-Doppler modulation present due to recoil as well, but our hypothesis is that signature will not be unique to this event (i.e. can be due to the presence of wind or flight dynamics). Whereas, the recoil-counter recoil effect is enforced upon the whole platform, hence it can be understood the bulk Doppler signature will be more distinctive. The lower Doppler sampling rate for FMCW operation corresponds to higher Doppler resolution. This is preferred as the bulk velocity due to impulse effect is expected to be quite low (in the range of $<5 \text{ ms}^{-1}$) [23]. Data was collected at both 24 and 94 GHz. The Doppler parameters for 24 GHz were the same as for the heavy payload analysis. For 94 GHz, the STFT length of displacement, the 94 GHz radar collected data with 10 cm range resolution. The 24 GHz radar has a more limited bandwidth and was operated with 1 m range resolution.

We collected experimental data on a DJI Phantom 3 Standard drone subject to a sudden inertial force. As it was not possible to use a real gun due to logistical and safety reasons, we imparted impulses to the drone by pulling it sharply several times using a wire. The wire was a few 2048 chirps corresponds to 164.8 milliseconds. The Doppler resolution is 6.1 Hz or 0.0097 ms^{-1} (at 94 GHz). To track the meters long with one end attached to the main body of the drone and the other end to the tip of a wooden pole. This pole was held upwards and by sharply pulling it backwards, an impulse was applied to the drone fuselage, thus simulating the recoil effect. Due to the drone's internal stabilisation mechanism, it then returned back to its previous position, which is the counter-recoil. Fig. 15 illustrates the entire experimental setup. The drone was hovering at $\sim 20 \text{ m}$ range.

For conciseness, we will focus on a single measurement run which was 14 s long. This dataset contains 5 impulse events. From the high range resolution profile (HRRP) data obtained by the 94 GHz radar, the impulse occurrences can be clearly seen in Fig. 16 (top). These have occurred at 2, 4, 6.5, 8.5 and 10 seconds. The displacement-time plot in Fig. 16 (bottom) is obtained by thresholding the drone returns from the noise floor and finding the median range within each range profile. The small positional changes are also observed, corresponding to about 3-4 range bins (30-40 cm). The other observation is that the change in range is quite brief and sharp when the force is applied (recoil) but is slightly longer when the drone is returning to its previous position (counter-recoil). Nonetheless, the changes in range are quite small even at such high resolution, implying that this may not be the ideal metric for detecting recoil.

We also analysed the Doppler signatures obtained from the same dataset. In Fig. 17 the FMCW-Doppler spectrograms again show the 5 impulse events quite clearly for the simultaneous data collected at 24 and 94 GHz. The effect of the impulses on the bulk Doppler of the drone is very distinct in every case, exhibiting a very rapid increase in positive velocity (away from the radar) during the applied impulse followed by a slower recovery with some negative velocity

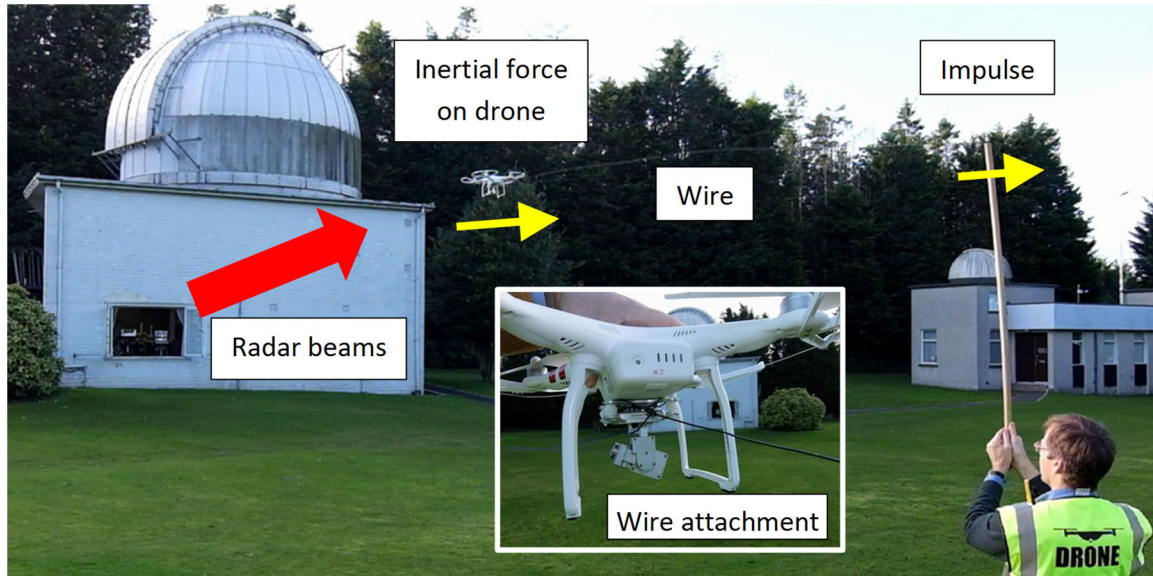


FIGURE 15. Experimental setup for collecting radar signatures of recoil and counter-recoil effect on drone.

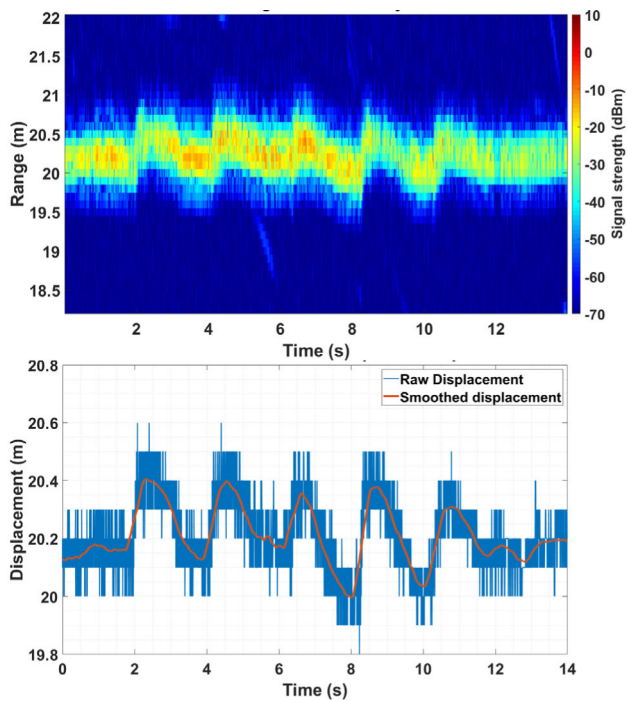


FIGURE 16. High range resolution profiles (94 GHz, 10 cm range bins) for measurement run containing 5 impulse events (top) and range-time plot of the median position of the drone returns (bottom).

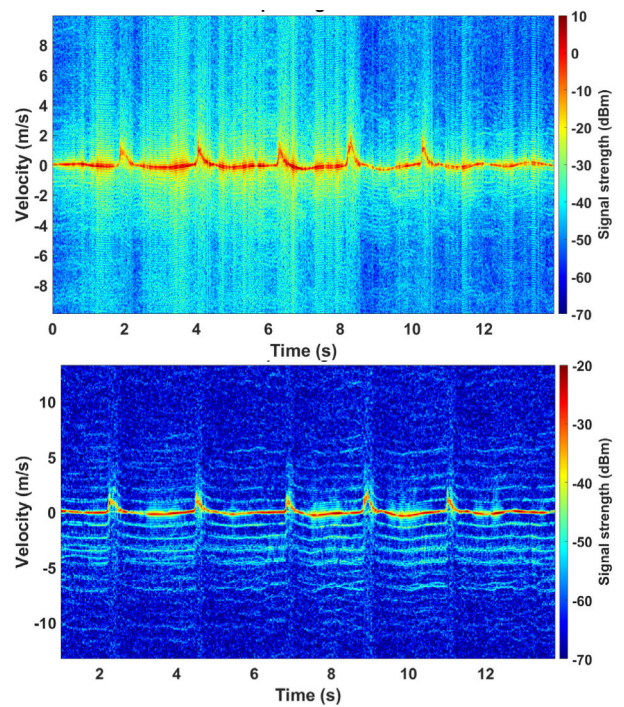


FIGURE 17. FMCW-Doppler spectrogram of drone subject to 5 impulse events at $t = 2, 4, 6.5, 8.5$ and 10 seconds measured at 94 GHz (top) and 24 GHz (bottom).

(towards the radar) as it attempts to re-stabilise and return to its nominal GPS position.

Fig. 18 presents the same 94 GHz data as Fig. 17 (top) but zoomed in on the velocity axis to highlight the behaviour of the bulk Doppler. The five impulse events can be seen very clearly as characteristic changes in the velocity of the drone. To quantify this velocity-time behaviour of the drone we extracted the points with maximum intensity (blue trace in Fig. 18 (bottom)) then smoothed them using a moving

average to reduce noise. To prevent the averaging process from suppressing the high velocity values around the sharp peaks, a local interpolation was applied (red trace in Fig. 18 (bottom)). This gives an accurate representation of the velocity versus time of the drone fuselage. From the velocity-time profile, the displacement-time profile can be calculated by numerical integration and this is shown in Fig. 19 (top). One can see the drone moves approximately $20 - 30$ cm (i.e. $2 - 3$ range bins) with each impulse, in broad agreement with the

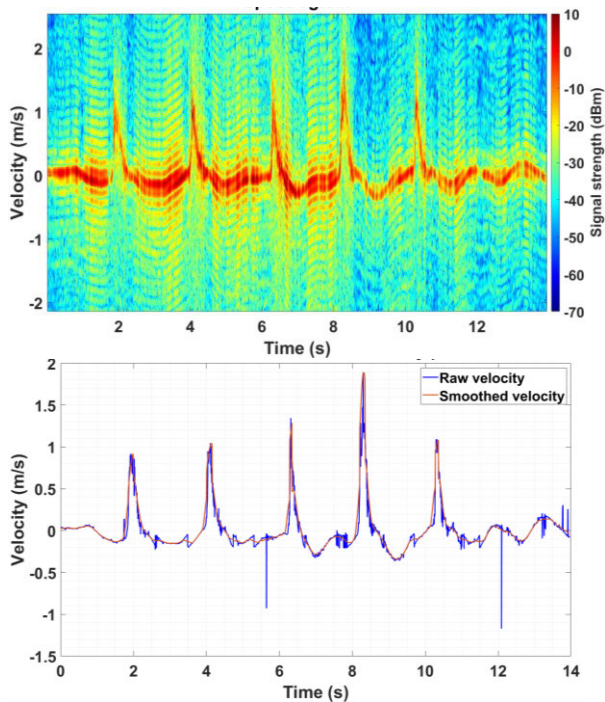


FIGURE 18. Zoomed in 94 GHz FMCW-Doppler spectrogram of drone subject to 5 impulse events (top) and velocity-time profile obtained by tracing the bulk velocity from the spectrogram (bottom). The smoothed trace is obtained by using a moving average and local interpolation to maintain the peak values.

HRRP data of Fig. 16. The net position of the drone appears to have changed by 30 cm over the course of the measurement run which may be an artefact of the integration process and this behavior is not shown in the HRRP data of Fig. 16. From the velocity-time profile the force-time profile can be calculated using $\text{force} = \text{mass} \times \text{acceleration}$. The mass is that of the drone (1.2 kg) and the acceleration is obtained by differentiating the velocity-time profile. The force-time profile is shown in blue in Fig. 19 (bottom) along with the velocity-time profile in red. All 5 impulse events exhibit the same characteristic shape in the force-time profile. The fourth impulse was notably more powerful than the others, reaching a peak force of 13.9 N whilst the others were about 6 N. Fig. 20 shows a close up of impulse #4 to illustrate the details of this signature. The impulse (labelled ‘recoil’) takes place over a few hundred milliseconds, characteristic of the stick and wire jerk technique, and is followed by a longer, damped oscillation, stabilisation and recovery process (labelled ‘counter-recoil’) which is characteristic of the drone’s flight controller properties. Key parameters for each impulse event were calculated from the velocity-time and force-time profiles as follows and displayed in Table 2:-

- *Impulse Time* – the time between the impulse starting (chosen manually) and the force passing through zero after the maximum value in the force-time profile. Note this also corresponds to the time taken for the velocity to increase from the baseline level up to the peak value.
- *Peak Velocity* – the maximum velocity at the top of the recoil peak in the velocity-time profile.

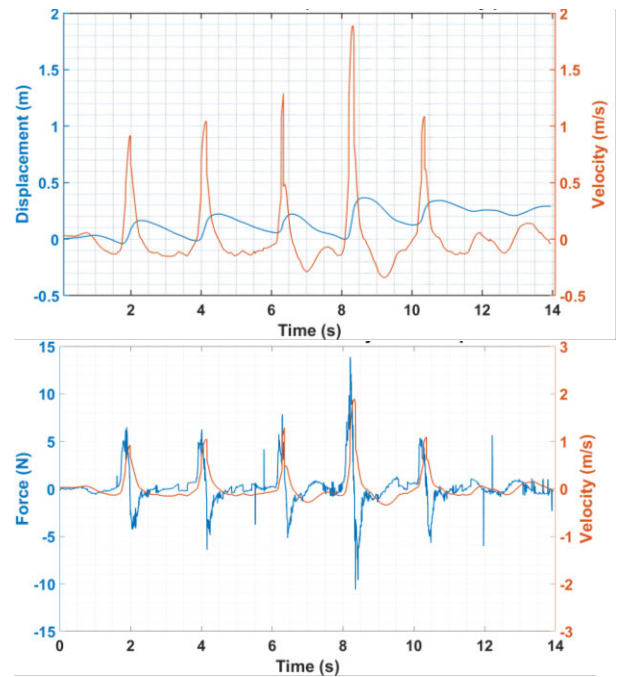


FIGURE 19. Displacement-time profile obtained from the smoothed velocity-time profile by numerical integration (top) and force-time profile obtained from the velocity-time profile (bottom).

TABLE 2. Calculated recoil parameters for the five impulses shown in Fig. 19. DJI phantom 3 weight is 1.2 kg.

#	Impulse Time (ms)	Peak Velocity (m/s)	Peak Force (N)	Recoil Impulse (N.s)	Recoil Energy (J)
1	328.8	0.92	6.50	1.10	0.51
2	296.3	1.05	6.26	0.95	0.66
3	279.2	1.29	7.86	0.84	1.01
4	338.1	1.90	13.90	1.71	2.17
5	248.3	1.09	5.35	0.79	0.71

- *Peak Force* – the maximum force at the top of the recoil peak in the force-time profile.
- *Recoil Impulse* – the area under the force-time profile for the duration of the impulse time. Impulse is defined as $\text{mass} \times \text{change in velocity}$.
- *Recoil Energy* – the kinetic energy $E = \frac{1}{2}mv_{pk}^2$ where m is the drone mass (1.2 kg) and v_{pk} is the peak velocity.

A. COMPARISON WITH PISTOL RECOIL

The method used to impart an impulse on the drone using a wire and pole has been compared with the recoil which might be imparted by a firearm, specifically a pistol which could feasibly be carried by a drone. The recoil properties of a Glock 22 pistol (weight 0.65 kg) firing a 9 mm parabellum round are quoted as [24]: Recoil Impulse 3.5 N.s, Recoil Velocity 5.3 ms^{-1} and Recoil Energy 9.3 J.

Whilst the duration of the impulse imparted by a pistol would be much shorter than that performed in the above experiments, the Recoil Impulse can be compared because that represents the total force-time product. Taking impulse #4 as the most powerful case, this exhibited a Recoil Impulse of 1.71 N.s which is nearly within a factor of two of the value for the Glock pistol.

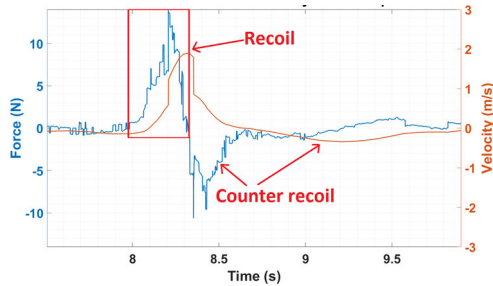


FIGURE 20. Close up of impulse #4 force-time and velocity-time profiles showing recoil and counter-recoil regimes.

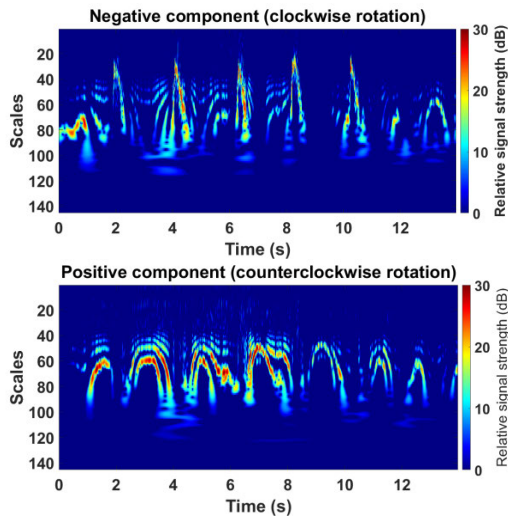


FIGURE 21. Scalogram plots of the drone subject to impulse events, showing strong signatures mostly when recoil and counter-recoil occurs.

Now consider the situation in which a Glock 22 is rigidly attached to a Phantom 3 and fires a 9 mm round, ignoring rotational or frictional forces. The Recoil Impulse available is still 3.5 N.s, the same as that exhibited by the pistol alone, but the mass has increased to 1.85 kg so the Recoil Velocity would be 1.89 ms^{-1} and the Recoil Energy would be 3.3 J. The experimentally achieved velocity and energy for impulse #4 are reasonably comparable with the values calculated for the drone-mounted pistol so we suggest they can be considered as being of a relevant order of magnitude.

As the bulk Doppler signature exhibits transient characteristic, we have also applied Continuous Wavelet Transform (CWT) analysis to the same complex time series data. Wavelet transformation is a very useful tool for analyzing such data where there is a presence of brief impulses [25]–[27]. The CWT based method has been applied previously to CW radar data to analyze the micro-Doppler signatures of drone propeller blades and bird wing beats for classification purposes [28]. Here, we are using similar method for recoil data analysis. The CWT scalogram is generated using the commonly chosen Morse wavelet which is useful for analyzing local discontinuities, where the symmetry parameter is defined as 3 and the time-bandwidth product is 60. The minimum and maximum scales are generated automatically with respect to the energy distribution in both

frequency and time domain. Fig. 21 shows the scalogram plots for both the anti-analytic part (negative component) and the analytic part (positive component). These scalograms differentiate between the recoil and counter-recoil as the velocity vectors are opposite in each case. The main observation here is that the signal strength is quite high during this impulse events ($>20 \text{ dB}$) compared to the signals not related to impulse. One problem is, signal similar to Fig. 21 (bottom) might be observed if the drone is moving from its nominal position due to other external factor (i.e. wind). So, to reliably detect, it is important to find a counter-recoil signature with a preceding recoil signature. The advantage of wavelet transform is that it has lesser computational load, $O(n)$, compared to Fourier transform, $O(n \log_2(n))$.

IV. CONCLUSION

This study aimed to gain a better understanding of the radar signatures of drones equipped with simulated threat payloads through the analysis of high fidelity experimental data. Careful consideration was given during the experimental trials to account for various external factors, such as wind speed, that could affect the radar signatures. High performance radars at 24 and 94 GHz with very good Doppler sensitivity were used to collect both FMCW and CW data. Robust signal processing was then applied to accurately analyze the data.

Our principal conclusions are as follows:-

1) The HERM lines evident in long integration spectrograms did not show any consistent unique signatures (e.g. degree of fluctuation or straightness) that are solely attributable to a drone carrying a payload rather than the effect of wind.

2) The blade flashes revealed in fully sampled, short integration spectrograms show the propeller tip velocity and rotation rate increase with payload weight. Whilst sudden changes in these parameters are more obvious when a payload is released, the signature is not uniquely caused by payloads so cannot be used as the sole basis of a classification algorithm. *A priori* knowledge of the drone and/or other sensor data (e.g. RF sensor to identify drone type, anemometer to measure wind speed) could be used in conjunction with the radar data to aid classification.

3) A sudden inertial force, like a bullet fired from a hand gun attached to the drone, produces a very distinctive signature which is revealed in high resolution Doppler data. Experimental results showed a characteristic spike in the bulk Doppler signature of the fuselage due to recoil, followed by a longer, damped oscillation effect due to counter-recoil caused by the flight controller restabilizing the platform. This signature is sufficiently distinctive that it could form the basis of a classification algorithm. We have also shown that wavelet analysis has the potential to be more sensitive to such impulse signatures and thus can enhance the system's ability to detect such event.

These results broaden the understanding of the radar signatures of drones equipped with various threat payloads and open doors for further research work. The use of sensor fusion

to combine radar measurements of propeller tip velocity and/or dominant rotation rate with data from other sensors (e.g. RF identification of drone type) could form the basis for classifying heavy payloads. Millimeter wave radar has the advantage over lower frequency systems of better Doppler sensitivity and resolution for a given coherent processing interval, which can be very useful for rapid high fidelity Doppler based payload classification. However, millimeter wave radars tend to be more limited in terms of range coverage. Hence, for practical operation, it might be useful to use radars at two different frequencies, a lower frequency one for target detection and tracking plus a higher frequency one for payload classification. Our simulated recoil signatures presented here are quite distinct and show promise as the basis for classification so it would be very beneficial to perform an experimental validation using a real drone-mounted firearm. Such progress in understanding the radar signatures of drone equipped with threat payloads and how they can be used for classification will be of value to designers developing counter-drone radar systems.

ACKNOWLEDGMENT

The views and conclusions contained in this document are those of the authors and should not be interpreted as representing the official policies, either expressed or implied, of the Army Research Laboratory or the U.S. Government.

REFERENCES

- [1] *Warning Over Terrorist Attacks Using Drones Given By EU Security Chief*. Accessed: Feb. 25, 2020. [Online]. Available: <https://www.forbes.com/sites/zakdoffman/2019/08/04/europes-security-chief-issues-dire-warning-on-terrorist-threat-from-drones/#6da839877ae4>
- [2] *Drones of Mass Destruction: Drone Swarms and the Future of Nuclear, Chemical, and Biological Weapons*. Accessed: Feb. 25, 2020. [Online]. Available: <https://warontherocks.com/2019/02/drones-of-mass-destruction-drone-swarms-and-the-future-of-nuclear-chemical-and-biological-weapons/>
- [3] J. de Wit, "Micro-Doppler analysis of small UAVs," in *Proc. 9th Eur. Radar Conf.*, Amsterdam, The Netherlands, Oct./Nov. 2012, pp. 210–213.
- [4] P. Molchanov, R. I. A. Harmanny, J. J. M. de Wit, K. Egiazarian, and J. Astola, "Classification of small UAVs and birds by micro-Doppler signatures," *Int. J. Microw. Wireless Technol.*, vol. 6, nos. 3–4, pp. 435–444, Jun. 2014.
- [5] M. Ritchie, F. Fioranelli, H. Griffiths, and B. Torvik, "Monostatic and bistatic radar measurements of birds and micro-drone," in *Proc. IEEE Radar Conf.*, May 2016, pp. 1–5.
- [6] F. Hoffmann, M. Ritchie, F. Fioranelli, A. Charlish, and H. Griffiths, "Micro-Doppler based detection and tracking of UAVs with multistatic radar," in *Proc. IEEE Radar Conf.*, May 2016, pp. 1–6.
- [7] D. A. Brooks, O. Schwander, F. Barbaresco, J.-Y. Schneider, and M. Cord, "Temporal deep learning for drone micro-Doppler classification," in *Proc. 19th Int. Radar Symp. (IRS)*, Jun. 2018, pp. 1–10.
- [8] J. S. Patel, F. Fioranelli, and D. Anderson, "Review of radar classification and RCS characterisation techniques for small UAVs or drones," *IET Radar, Sonar Navigat.*, vol. 12, no. 9, pp. 911–919, Sep. 2018.
- [9] V. C. Chen, *The Micro-Doppler Effect in Radar*. Norwood, MA, USA: Artech House, 2011.
- [10] M. Ritchie, F. Fioranelli, H. Borrión, and H. Griffiths, "Multistatic micro-Doppler radar feature extraction for classification of unloaded/loaded micro-drones," *IET Radar, Sonar Navigat.*, vol. 11, no. 1, pp. 116–124, Jan. 2017.
- [11] J. S. Patel, C. Al-Ameri, F. Fioranelli, and D. Anderson, "Multi-time frequency analysis and classification of a micro-drone carrying payloads using multistatic radar," *J. Eng.*, vol. 2019, no. 20, pp. 7047–7051, Oct. 2019.
- [12] Y. Zhao, X. Zhang, and F. Fioranelli, "Initial results of radar-based classification of commercial drone carrying small payloads," in *Proc. Int. Radar Conf.*, Sep. 2019.
- [13] S. Rahman and D. A. Robertson, "Millimeter-wave micro-Doppler measurements of small UAVs," in *Proc. SPIE*, vol. 10188, May 2017, Art. no. 101880T.
- [14] S. Rahman and D. A. Robertson, "Coherent 24 GHz FMCW radar system for micro-Doppler studies," *Proc. SPIE Radar Sensor Technol.*, vol. 10633, May 2018, Art. no. 106330I.
- [15] D. A. Robertson, G. M. Brooker, and P. D. L. Beasley, "Very low-phase noise, coherent 94GHz radar for micro-Doppler and vibrometry studies," in *Proc. SPIE*, vol. 9077, May 2014, Art. no. 907719.
- [16] S. Rahman and D. A. Robertson, "Millimeter-wave radar micro-Doppler feature extraction of consumer drones and birds for target discrimination," *Proc. SPIE Radar Sensor Technol.*, vol. 11003, May 2019, Art. no. 110030S.
- [17] J. J. M. de Wit, R. I. A. Harmanny, and P. Molchanov, "Radar micro-Doppler feature extraction using the singular value decomposition," in *Proc. Int. Radar Conf.*, Oct. 2014, pp. 1–6.
- [18] S. Rahman and D. A. Robertson, "Classification of drones and birds using convolutional neural networks applied to radar micro-Doppler spectrogram images," *IET Radar, Sonar Navigat.*, vol. 14, no. 5, pp. 653–661, May 2020.
- [19] B. K. Kim, H.-S. Kang, and S.-O. Park, "Drone classification using convolutional neural networks with merged Doppler images," *IEEE Geosci. Remote Sens. Lett.*, vol. 14, no. 1, pp. 38–42, Jan. 2017.
- [20] D. Choi and B. Oh, "Classification of drone type using deep convolutional neural networks based on micro-Doppler simulation," in *Proc. Int. Symp. Antennas Propag.*, Busan, South Korea, Oct. 2018, pp. 1–2.
- [21] C. Szegedy, W. Liu, Y. Jia, P. Sermanet, S. Reed, D. Anguelov, D. Erhan, V. Vanhoucke, and A. Rabinovich, "Going deeper with convolutions," in *Proc. IEEE Conf. Comput. Vis. Pattern Recognit. (CVPR)*, Jun. 2015, pp. 1–9.
- [22] M. A. Govoni, "Micro-Doppler signal decomposition of small commercial drones," in *Proc. IEEE Radar Conf. (RadarConf)*, May 2017, pp. 0425–0429.
- [23] M. J. Hall, "Effects of breech bolt movement on felt recoil of a gas-operated semi-automatic sporting gun," *Proc. Inst. Mech. Engineers, Part P: J. Sports Eng. Technol.*, vol. 229, no. 3, pp. 159–168, Sep. 2015.
- [24] *Recoil*. Entry in Wikipedia. Accessed: May 1, 2020. [Online]. Available: <https://en.wikipedia.org/wiki/Recoil>
- [25] V. C. Chen and R. D. Lipps, "Time frequency signatures of micro-Doppler phenomenon for feature extraction," *Proc. SPIE Wavelet Appl.*, vol. 4056, pp. 220–226, May 2000.
- [26] T. Thayaparan, S. Abrol, E. Riseborough, L. Stankovic, D. Lamothe, and G. Duff, "Analysis of radar micro-Doppler signatures from experimental helicopter and human data," *IET Radar, Sonar Navigat.*, vol. 1, no. 4, p. 289, 2007.
- [27] S. Zhang, J. Fan, L. Shou, and J. Dong, "A detection method of radar signal by wavelet transforms," in *Proc. 4th Int. Conf. Fuzzy Syst. Knowl. Discovery (FSKD)*, 2007, pp. 710–714.
- [28] S. Rahman and D. Robertson, "Time-frequency analysis of millimeter-wave radar micro-Doppler data from small UAVs," in *Proc. Sensor Signal Process. Defence Conf. (SSPD)*, Dec. 2017, pp. 1–5.



SAMIUR RAHMAN (Member, IEEE) received the M.Sc. degree in electrical engineering from the Blekinge Institute of Technology, Sweden, in 2010, and the Ph.D. degree from University College London (UCL), U.K., in 2015. Since his Ph.D., he has been working as a Research Fellow with the Millimetre Wave Group, University of St Andrews, U.K. His research interests include radar imaging techniques, radar target classification algorithm development, radar target signature analysis, radar signature modeling, and millimetre-wave radar system design.



DUNCAN A. ROBERTSON (Member, IEEE) received the B.Sc. degree (Hons.) in physics and electronics and the Ph.D. degree in millimetre wave physics from the University of St Andrews, U.K. For most of his career, he has been with the Millimetre Wave Group, University of St Andrews, working on battlefield systems, passive imaging, electron spin resonance spectroscopy instrumentation, and millimetre wave radar for remote sensing and security applications.

His research interests include millimetre-wave radar, radiometry, imaging, electron spin resonance instrumentation, quasi-optics, and materials characterization and antennas.



MARK A. GOVONI (Senior Member, IEEE) received the B.S.E. and M.S. degrees from Arizona State University, Tempe, AZ, USA, in 2000 and 2001, respectively, and the Ph.D. degree from the Stevens Institute of Technology, Hoboken, NJ, USA, in 2011. He has authored or coauthored more than 100 technical publications/documents, including one book chapter and holds seven patents. His research interests include radar signal processing, radar phenomenology, radar waveform design, and radar system optimization techniques.

• • •